Zhiyong Wang, Zhen Zhang, Haoyuan Qi, Andres Ortega-Guerrero, Lihuan Wang, Kun Xu, Mingchao Wang, SangWook Park, Felix Hennersdorf, Arezoo Dianat, Alexander Croy, Hartmut Komber, Gianaurelio Cuniberti, Jan J. Weigand, Ute Kaiser, Renhao Dong, Xinliang Feng

On-water surface synthesis of charged two-dimensional polymer single crystals via the irreversible Katritzky reaction

Erstveröffentlichung in / First published in:

Nature Synthesis. 2021, 1, S. 69–76. Springer Nature. ISSN 2731-0582.

DOI: https://doi.org/10.1038/s44160-021-00001-4

Final edited form was published in "Nature Synthesis". 1 S. 69-76. ISSN: 2731-0582.
https://doi.org/10.1038/s44160-021-00001-4

On-Water Surface Synthesis of Charged Two-Dimensional Polymer Single Crystals via the Irreversible Katritzky Reaction

Zhiyong Wang[1,5,6], Zhen Zhang[1,6], Haoyuan Qi[1,3,6], Andres Ortega-Guerrero[2], Lihuan Wang[1], Kun Xu[1], Mingchao Wang[1], SangWook Park[1], Felix Hennersdorf[4], Arezoo Dianat[2], Alexander Croy[2], Hartmut Komber[5], Gianaurelio Cuniberti[2], Jan J. Weigand[4], Ute Kaiser[3], Renhao Dong[1]*, and Xinliang Feng[1]*

[1]Center for Advancing Electronics Dresden & Faculty of Chemistry and Food Chemistry, Technische Universität Dresden, Dresden, Germany.

[2]Institute for Materials Science and Max Bergmann Center of Biomaterials and Center for Advancing Electronics Dresden, Technische Universität Dresden, Dresden, Germany.

[3]Central Facility for Electron Microscopy, Electron Microscopy of Materials Science, Universität Ulm, Ulm, Germany.

[4]Chair of Inorganic Molecular Chemistry, Technische Universität Dresden, Dresden, Germany.

[5]Leibniz-Institut für Polymerforschung Dresden e. V., Dresden, Germany.

[6]These authors contributed equally: Zhiyong Wang, Zhen Zhang, Haoyuan Qi

*E-mail: renhao.dong@tu-dresden.de; xinliang.feng@tu-dresden.de

Final edited form was published in "Nature Synthesis". 1 S. 69-76. ISSN: 2731-0582.
https://doi.org/10.1038/s44160-021-00001-4

Synthetic two-dimensional polymers (2DPs) and their layer-stacked 2D covalent organic frameworks (2D COFs) have emerged as a class of structurally defined crystalline polymer materials with exotic physical and chemical properties. Yet, synthesizing 2DP and 2D COF single crystals via irreversible reactions still remains an immense challenge. Here, we report the synthesis of skeleton-charged 2DP single crystals (C2DP-Por, C2DP-ZnPor, and C2DP-Py) through an irreversible Katritzky reaction under pH control on the water surface, which presents a new type of linkage chemistry for the 2DP and 2D COF families. The resultant periodically ordered 2DPs comprise aromatic pyridinium cations and counter BF_4^- anions. The representative C2DP-Por crystals display a tunable thickness of 2-30 nm and a lateral size up to 120 μm^2, which far exceeds the thus-far reported 2DPs and 2D COFs synthesized by irreversible bonds. Square lattice with $a = b = 30.5$ Å is resolved by imaging and diffraction methods with near-atomic precision. Intrigued by the cationic polymer skeleton and columnar-like pore arrays, we further integrate the C2DP-Por crystals into an osmotic power generator device that exhibits an excellent chloride ion selectivity with a coefficient value reaching ~ 0.9 and a high output power density of 4 W m^{-2}, superior to other 2D materials such as graphene and boron nitride. These findings open up possibilities for developing single-crystalline 2DPs via irreversible reaction and their applications in energy conversion technologies.

Recent advances on synthetic polymer crystals have witnessed the rise of single- to few-layer two-dimensional polymers (2DPs) and their van der Waals layer-stacked 2D covalent organic frameworks (2D COFs)[1,2]. These porous crystalline polymers have displayed diverse physical and chemical properties for broad functions in optoelectronics, spintronics, membrane, catalysis, and energy storage and conversion[3]. To achieve such crystalline polymer materials, dynamic covalent

Final edited form was published in "Nature Synthesis". 1 S. 69-76. ISSN: 2731-0582.
https://doi.org/10.1038/s44160-021-00001-4

chemistry (DCC) has been commonly utilized, such as boronic ester reaction[4,5], Schiff-base reaction[6,7] and imidization reaction[8]. These reversible reactions allow bonds to form, break, and reform, associated with molecular exchange under thermodynamic equilibrium conditions[9], thus enabling a defect self-correction to make long-range ordered 2D networks[10,11]. Despite the growing interest in the synthesis of 2DPs and 2D COFs via DCC, the reversible nature of the bonding inevitably limits their structural and functional diversities as well as stabilities.

The utilization of kinetically irreversible reactions for the synthesis of 2DPs and 2D COFs is highly attractive but remains challenging. Recently, Knoevenagel[12,13], Aldol-type and Horner-Wadsworth-Emmons condensation reactions[14-16] have been developed for the solvothermal synthesis of vinylene-linked 2D COFs, affording fully conjugated polymer materials with high chemical and thermal stabilities. On the other hand, surface-binding structurally-defined conjugated 2DPs have been realized via the on-surface Ullmann coupling under ultrahigh vacuum conditions[17-20]. Nevertheless, these approaches have remained limited to making microcrystalline polymer products with domain size up to dozens of nanometers, posing a potential limitation for the sample processing and device integration as well as the development of reliable functions.

Here, we report the on-water surface synthesis of few-layer, large-area, single crystalline cationic 2DPs (**C2DPs**) (**C2DP-Por**, **C2DP-ZnPor**, and **C2DP-Py**) by irreversible Katritzky reaction of metal-free or Zn(II) 5,10,15,20-(tetra-4-aminophenyl) porphyrin) (**9** or **10**) or 1,3,6,8-tetrakis(4-aminophenyl)pyrene (**12**) with 1,4-phenylene-4,4'-bis(2,6-diphenyl-4-pyrylium tetrafluoroborate (**11**) assisted by surfactant monolayer. Representatively, the synthetic **C2DP-Por** single crystals display a tunable thickness of ~ 2-30 nm and a record lateral size up to 120 μm^2. The crystal structure with the atomic precision is determined by high-resolution transmission electron microscopy (HRTEM) imaging and grazing incidence wide-angle X-ray scattering

Final edited form was published in "Nature Synthesis". 1 S. 69-76. ISSN: 2731-0582.
https://doi.org/10.1038/s44160-021-00001-4

(GIWAXS), revealing a highly uniform square-patterned structure with the in-plane lattice of a = b = 30.5 Å. The intrinsic positively charged skeleton that are balanced by BF_4^- counter ions is further supported by the spectroscopic characterization and single crystal structure analysis of a corresponding model compound. Probing interfacial ring-transmutation polymerization mechanism, assisted by theoretical calculation and model reaction, unveils that manipulating pH in ring opening and ring closure steps enables the control of the reaction kinetics toward the final **C2DP** structures. As a consequence, we successfully demonstrate the synthetic approach toward achieving 2DP single crystals by irreversible reactions under kinetic control. Furthermore, we integrate the resultant **C2DP-Por** as an anion-selective membrane for osmotic energy generation. The cationic backbone and well-defined quasi-1D channels offer a high chloride ion selectivity with a coefficient up to 0.9, and an output power density as high as 4.0 W m^{-2} that outperforms the state-of-art 2D materials such as graphene[21] and boron nitride[22].

Results and discussion

Chemistry of irreversible Katritzky reaction on the water surface. Katritzky reaction of bispyrylium salts with aromatic, heterocyclic, or aliphatic diamines has been widely used to synthesize linear poly(pyridinium salt)s as a kind of ionic polymers[23]. This reaction involves pH-manipulative reversible ring opening and irreversible ring closure, which is generally considered as a kinetically controlled reaction[24,25]. To examine the feasibility of this irreversible reaction for the on-water surface polymerization, we evaluated a model reaction (named as **Model-1-I**) between 5-(4-aminophenyl)-10,15,20-(triphenyl)porphyrin (**1**) and 2,4,6-triphenylpyrylium tetrafluoroborate (**2**) assisted by a surfactant monolayer with a dynamic pH control (Fig. 1a). The reaction was enabled with three steps, including surfactant monolayer guided preorganization of compound **1**, Lewis base-catalyzed reversible ring opening, and acid-catalyzed irreversible ring

4

Final edited form was published in "Nature Synthesis". 1 S. 69-76. ISSN: 2731-0582.
https://doi.org/10.1038/s44160-021-00001-4

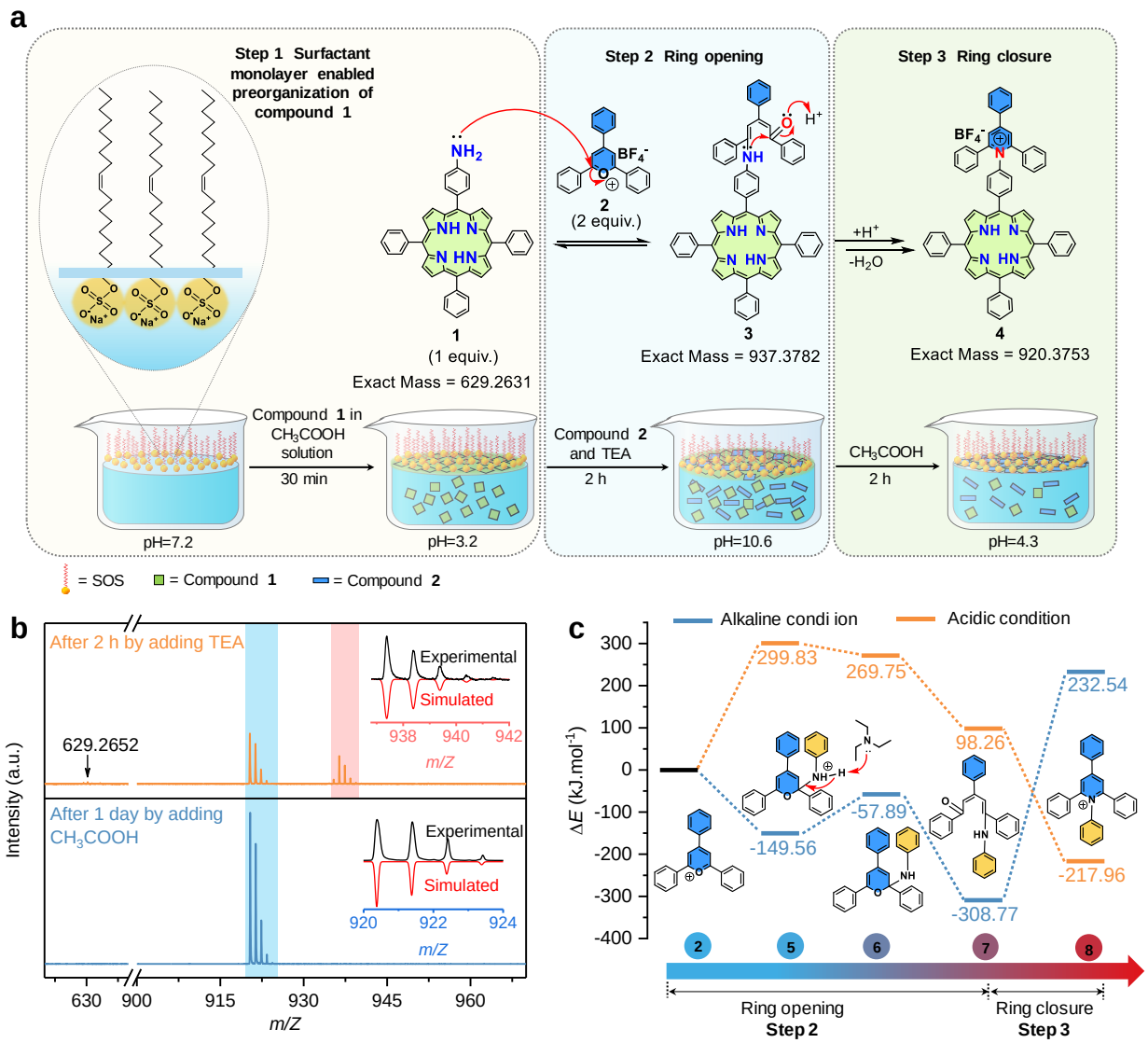

Fig. 1 | Chemistry of irreversible ring-transmutation reaction on the water surface. a, The model reaction between compounds **1** and **2** yields **4**, and a schematic illustration of the synthetic procedure through surfactant monolayer assisted interfacial synthesis (SMAIS) method. **b**, MALDI-TOF MS analysis of **Model-1-I** after 2 h by adding compound **2** and after 1 day by adding CH_3COOH, respectively. **c**, Calculated reaction energy diagram in the conversion of pyrylium into pyridinium salts. All total energies are with respect to **2**. Compounds **5**, **6**, **7**, **8** represent *a*-C adduct, 2H-pyran intermediate, vinylogous amide, and pyridinium, respectively.

Final edited form was published in "Nature Synthesis". 1 S. 69-76. ISSN: 2731-0582.
https://doi.org/10.1038/s44160-021-00001-4

closure. In Step 1, a sodium oleyl sulfate (SOS) monolayer is prepared on the water surface in a beaker (diameter, 6 cm)[8]. After 30 min, a mixed aqueous solution (1 mL) of CH_3COOH (1.75 mmol) and compound **1** (7.9×10^{-4} mmol) is injected into the water subphase (pH reaches to 3.2 after the injection). Due to the electrostatic interaction between the protonated compound **1** and the anionic head groups of SOS, compound **1** is readily adsorbed underneath the SOS monolayer. After 2 h, an aqueous solution of compound **2** (7.9×10^{-4} mmol, 1 mL) is injected into the water subphase (Step 2 in Fig. 1a). Subsequently, the pH of the reaction solution is adjusted to 10.6 by the addition of triethylamine (TEA, 1.75 mmol) to promote the ring opening for 2 h. In Step 3, we further tune the pH of solution to 4.3 by adding CH_3COOH (8.75 mmol), thus triggering the final ring closure step. The reaction is kept at 1 °C under ambient condition for 1 day which affords a macroscopic red film on the water surface.

The reaction mechanism of **Model-1-I** is illustrated schematically in Fig. 1a and Supplementary Fig. 1. As the conversion from *a*-C adduct to 2H-pyran is undetectable by spectroscopic methods[25], the identification of ring opening intermediate **3** and target pyridinium product **4** is of importance to support the reaction procedure. We, therefore, performed matrix-assisted laser desorption/ionization time-of-flight mass spectrometric (MALDI-TOF MS) measurement to monitor the product evolution at Step 2 and Step 3 (Fig. 1b). The product film was collected from the water surface and rinsed by water, naturally dried, and then applied for the MS analysis. After 2 h reaction by adding TEA (Step 2), the MS spectrum presents sharp peaks at m/z = 937.3760 and m/z = 920.3749 (Fig. 1b, top), which are assigned to the intermediate compound **3** (m/z = 937.3782) and final product **4** (m/z = 920.3753), respectively. Besides, due to the reversibility of ring opening step, we also detected co-existed **1** at m/z = 629.2652. After the addition of CH_3COOH for 1 day (Step 3), the peak for **3** vanished whilst the peak at m/z =

Final edited form was published in "Nature Synthesis". 1 S. 69-76. ISSN: 2731-0582.
https://doi.org/10.1038/s44160-021-00001-4

920.3758 for **4** was recorded (Fig. 1b, bottom). We further collected the as-synthesized **4** and characterized its structure by ^{1}H NMR spectrometry and attenuated total reflectance Fourier transform infrared spectroscopy (ATR-FTIR) (Supplementary Fig. 2). For comparison, we also carried out the same model reaction with pH control in water solution without using a surfactant monolayer (named **Model-1-II**). In this case, the MS spectrum revealed an incomplete reaction with a low conversion degree for the products in the water phase, in which **3** and **4** always co-existed with a large amount of unreacted **1** and **2** (Supplementary Fig. 3). Therefore, the above contrast experiments suggest that the 2D confinement at the air/water interface supported by the surfactant monolayer, together with the pH control, is imperative for enhancing the reactivity of ring opening and ring closure.

Theoretical modelling of pH influence on the reaction kinetics. To understand the fundamental role of pH control in the ring-transmutation reaction, we calculate the reaction energy barriers in Step 2 (pH = 10.6) and Step 3 (pH = 3.2) through a density functional theory (DFT) method. To simplify the calculation, we substitute compound **1** by aniline that reacts with **2**. As shown in Fig. 1c, we observe that the alkaline condition is able to drastically reduce the energy barrier of the ring opening step (from compound **5** to **7**) to be -149.56 kJ mol^{-1}, -57.89 kJ mol^{-1} and -308.77 kJ mol^{-1}, respectively. This is due to the adjacent nitrogenous base, TEA, which can serve as a proton acceptor to strongly accelerate the deprotonation of 2*H*-pyran intermediate **6** (ref.[25,26]). However, in the subsequent ring closure from **7** to **8**, the related energy rises as high as 232.54 kJ mol^{-1}, indicating that the conversion from vinylogous amide to pyridinium via the ring closure is suppressed in the alkaline condition. In contrast, this ring closure reaction proceeds differently under the acidic condition. While the ring opening is inhibited with a higher reaction barrier of 98.26 kJ mol^{-1}, the acid-catalyzed ring closure exhibits a significantly lower reaction barrier of -

7

Final edited form was published in "Nature Synthesis". 1 S. 69-76. ISSN: 2731-0582.
https://doi.org/10.1038/s44160-021-00001-4

217.96 kJ mol^{-1} from **7** to **8**. Thus the acid can efficiently facilitate the rate-determining cyclodehydration. Therefore, the manipulation of pH in different reaction steps enables to promote the ring opening and ring closure, and finally accelerate the overall reaction on the water surface.

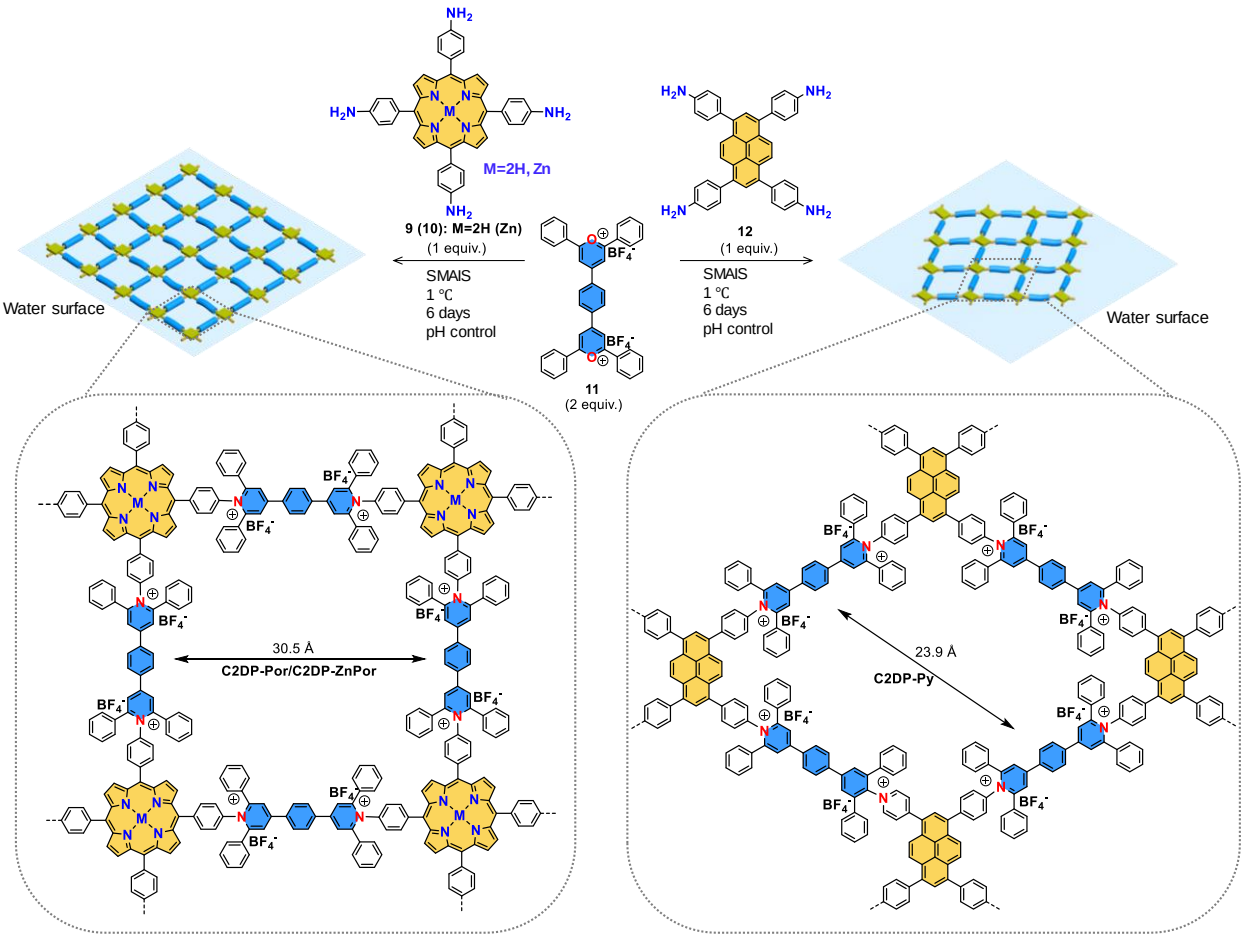

Fig. 2 | Schematic illustration of the reaction of **9** (M = 2H)/**10** (M = Zn) with **11** to form **C2DP-Por** and **C2DP-ZnPor** with a square lattice (a = b = 30.5 Å), as well as the reaction between **12** and **11** to form **C2DP-Py** with a centered rectangular lattice and a pore size of 23.9 Å.

Synthesis and characterization of C2DP-Por single crystals on the water surface. Based on the experimental observations and theoretical analyses of the kinetic pH control in promoting the Katritzky reaction, we then explored the synthesis of **C2DP** by (A_4+B_2)-type polycondensation reaction between monomers **9** and **11** under otherwise identical SMAIS condition but prolonged

8

Final edited form was published in "Nature Synthesis". 1 S. 69-76. ISSN: 2731-0582.
https://doi.org/10.1038/s44160-021-00001-4

the reaction time to 6 days (Fig. 2, left). The synthetic **C2DP-Por** film (~ 28 cm^2 in size) on the water surface was transferred horizontally onto different substrates for morphological and structural characterizations. As shown in Fig. 3a, b, we observed plentiful large **C2DP-Por** single crystals on the thin films, and the size distribution maintains monomodal with large domain size (40-100 μm^2). Atomic force microscopy (AFM) measurement reveals a thickness of ~ 20 nm for the obtained **C2DP-Por** single crystals (Fig. 3c). We note that the average size and thickness of single crystals increases upon increasing reaction time (size = 1 ± 0.5 μm^2, thickness = 2 ± 0.4 nm after 1 day; and size = 120 ± 2.5 μm^2, thickness = 30 ± 1.2 nm after 10 days) (Supplementary Fig. 4). This presents a record domain size for the reported 2DPs and 2D COFs synthesized by the irreversible bonds[12,13]. The largest domain size corresponds to a molecular weight as high as ~ 2.75×10^{10} g mol^{-1}. In addition, due to the weak interlayer interaction caused by the electrostatic repulsion between the neighboring **C2DP** layers, the layer-stacked single crystals can be readily exfoliated through mechanical exfoliation by Scotch tape, which demonstrates the single sheet nature of **C2DP-Por** (Fig. 3d and Supplementary Fig. 5). As shown in Supplementary Fig. 6, after exfoliation, the **C2DP-Por** crystal has a step-like structure at the edge of the crystalline domains. The determined step heights of 0.8 ± 0.1 and 2.0 ± 0.2 nm can be assigned to the thickness of monolayer and bilayer, respectively.

The efficient conversion of the amine group and pyrylium into pyridinium linkage in **C2DP-Por** was confirmed by ATR-FTIR spectroscopy with the appearance of the pyridinium ring signal C-N^+ band at ~ 1,638 cm^{-1}, as well as the full vanishing of the N-H stretch (~ 3,350 cm^{-1}) from compound **9** and C-O vibration (~ 1,240 cm^{-1}) from compound **11**, respectively (Fig. 3e). Raman spectra recorded within the crystal domain show the emergence of a new peak at 1,595 cm^{-1}, verifying the formation of C-N^+ bonds (Supplementary Fig. 7). X-ray photoelectron spectroscopy

Final edited form was published in "Nature Synthesis". 1 S. 69-76. ISSN: 2731-0582.
https://doi.org/10.1038/s44160-021-00001-4

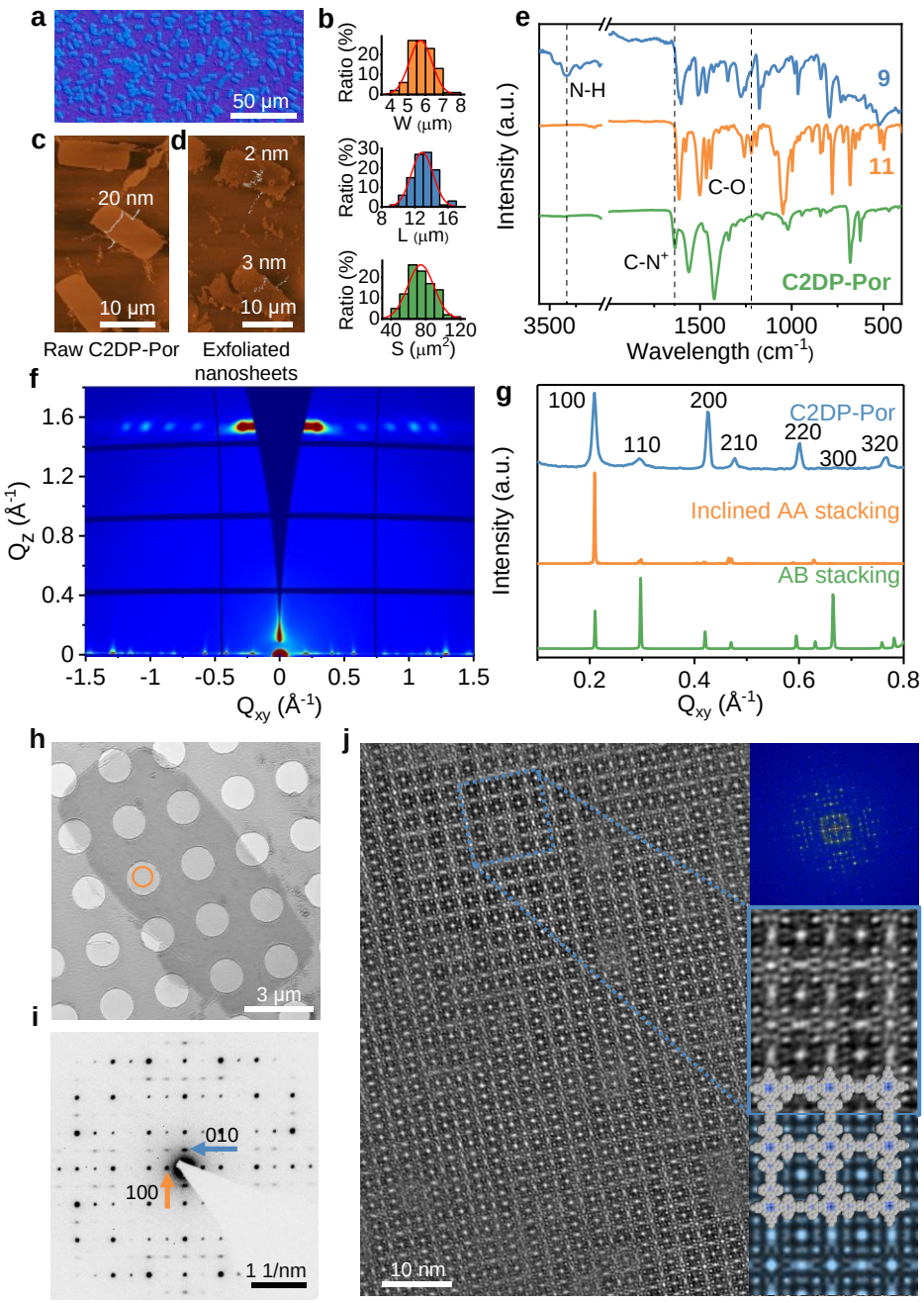

Fig. 3 | Morphological and structural characterizations of C2DP-Por film. a, Optical microscopy image of **C2DP-Por** film. **b**, The size distribution of crystals. **c**, AFM image of **C2DP-Por** film. The height profile of the crystals is marked in the image. **d**, AFM image of the exfoliated **C2DP-Por** crystals. **e**, ATR-FTIR spectra of monomer **9**, monomer **11,** and **C2DP-Por**. **f**, GIWAXS pattern of the **C2DP-Por** film (thickness, 30 nm). **g**, Experimental and calculated in-plane (near Q_z = 0) projections. **h**, An overview of the **C2DP-Por** film by bright-field TEM. **i**, SAED pattern from the marked crystalline domain in (**h**). **j**, Wiener-denoised AC-HRTEM image of **C2DP-Por** acquired with a total electron dose of 70 e^- Å^{-2}. Inset, top: corresponding FFT pattern. Inset, bottom: Magnified AC-HRTEM image of **C2DP-Por** and simulated AC-HRTEM image with structure overlaid (thickness: 20 nm, defocus: 420 nm).

10

Final edited form was published in "Nature Synthesis". 1 S. 69-76. ISSN: 2731-0582.
https://doi.org/10.1038/s44160-021-00001-4

(XPS) analysis reveals a distribution of C, N, and F in **C2DP-Por** (Supplementary Fig. 8). Quantitative analysis of the XPS presents a N^+ (atom%):F (atom%) ratio of 1:4.2 and a C (atom%):N (atom%) ratio of 15.1:1, which are in agreement with the composition of **C2DP-Por** (N^+/F = 1/4, C/N = 15.8/1). The resultant element ratio in **C2DP-Por** is also consistent with the single crystal analysis of model compound **13** (formula: $C_{136}H_{94}B_4F_{16}N_8$) that was synthesized from **9** and **2** in solution, indicating that each cationic N in the pyridinium ring is balanced by one counter ion BF_4^- (Supplementary Fig. 9-16).

To probe the crystallinity and lattice structure of **C2DP-Por**, we performed GIWAXS and TEM measurements on the synthetic thin films. As shown in Fig. 3f, the GIWAXS scattering pattern displays sharp and discrete Bragg spots near $Q_Z = 0$, indicating superior crystallinity on the macroscopic level. The in-plane peaks at $Q_y = 0.21$ and 0.42 $Å^{-1}$ correspond to the 100 and 200 Bragg reflections of a square lattice with $a = b = 30.5$ Å (Fig. 3g), agreeing well with the lattice structure of **C2DP-Por** derived by DFT calculation, and the single crystal structure of model compound **13** (Supplementary Fig. 16, Supplementary Table 1 and Table 2). An intense arc at 1.58 $Å^{-1}$ suggests a π-π stacking along the *c* direction with an interlayer distance of ~ 4.0 Å (Supplementary Fig. 17). The intensity profile resolved in the samples supports the AA-inclined stacking. On the microscopic scale, selected-area electron diffraction (SAED) reveals that each **C2DP-Por** flake is a single crystal without any detectable amorphous fragments (Supplementary Fig. 18). As shown in Fig. 3h, i, the square unit cell with the nearest reflections at 0.328 nm^{-1} further supports an AA-inclined stacking atomic model of **C2DP-Por** (Supplementary Fig. 19). AC-HRTEM images show a highly ordered square lattice with a lattice parameter of 30.5 Å (Fig. 3j). Noting that due to its high sensitivity to electron irradiation, **C2DP-Por** could undergo nontrivial structural disintegration during the imaging process (Supplementary Fig. 20). Therefore,

11

Final edited form was published in "Nature Synthesis". 1 S. 69-76. ISSN: 2731-0582.
https://doi.org/10.1038/s44160-021-00001-4

Wiener filtering was applied to the experimental image to remove the amorphous background. In Fig. 3j, the experimental image is in excellent agreement with the simulated one (Supplementary Fig. 21). The fast Fourier transform (FFT) image (Fig. 3j, inset) with a fourfold symmetry well reproduces the diffraction patterns disclosed in the experimental image.

Extend the interfacial irreversible Katritzky reaction toward C2DP-ZnPor and C2DP-Py. We further extended the reaction generality to the synthesis of **C2DP-ZnPor** (Fig. 2, left) and **C2DP-Py** (Fig. 2, right), respectively, by employing **10** and **11**, or **12** and **11** as monomer combinations under similar synthesis conditions. As shown in Supplementary Fig. 22, we achieved a large-area thin film of **C2DP-ZnPor** with crystal size in the range of 30-80 μm^2, and a tunable thickness of ~ 2.5-25 nm as a function of reaction time from 1 day to 6 days. The SAED pattern presents the first-order reflections at 0.328 nm^{-1} (Supplementary Fig. 23a), corresponding to a square unit cell with lattice constants of $a = b$= 30.5 Å, which is isostructural to **C2DP-Por**. HRTEM imaging illustrates the same square lattice with a lattice parameter of 30.5 Å (Supplementary Fig. 23b). GIWAXS measurement of **C2DP-ZnPor** shows an intensive π-π stacking peak at 1.61 $Å^{-1}$ along the out-of-plane direction, demonstrating an interlayer distance of ~ 3.9 Å (Supplementary Fig. 23c, d). In addition, **C2DP-Py** with centered rectangular lattice was synthesized with a domain size of 0.1 μm^2 and a thickness of 15 nm. We attribute the limited crystalline domain size of **C2DP-Py** to the vertical assembly of the D_{2h}-symmetric monomer **12** stemming from its hydrophobicity. More specifically, the hydrophilic ($-NH_2$) groups orient toward the water surface, while the hydrophobic pyrene core tends to leave out of the subphase, thereby enforcing the monomer **12** to stand energytically favorably on the water surface. The vertical alignment of **12** determines the subsequent nucleation and 2D polymerization process, thus facilitating the vertical growth and yielding **C2DP-Py** with limited lateral crystal domains. ATR-

12

Final edited form was published in "Nature Synthesis". 1 S. 69-76. ISSN: 2731-0582.
https://doi.org/10.1038/s44160-021-00001-4

FTIR measurement confirms the formation of pyridinium by the appearance of the C-N^+ characteristic peak (1,678 cm^{-1}), as well as the elimination of the N-H stretch (3,350 cm^{-1}) of **12** (Supplementary Fig. 24). As shown in Supplementary Fig. 25, the sharp SAED pattern reveals a linear reflection. The observed diffraction spots at 0.43 nm^{-1} confirm the pore size of 23.9 Å (23.2 Å/sin(76°)) in **C2DP-Py**. HRTEM image acquired perpendicularly to the [001] axis discloses a rhombic arrangement, and the lattice is determined to be 23.9 Å.

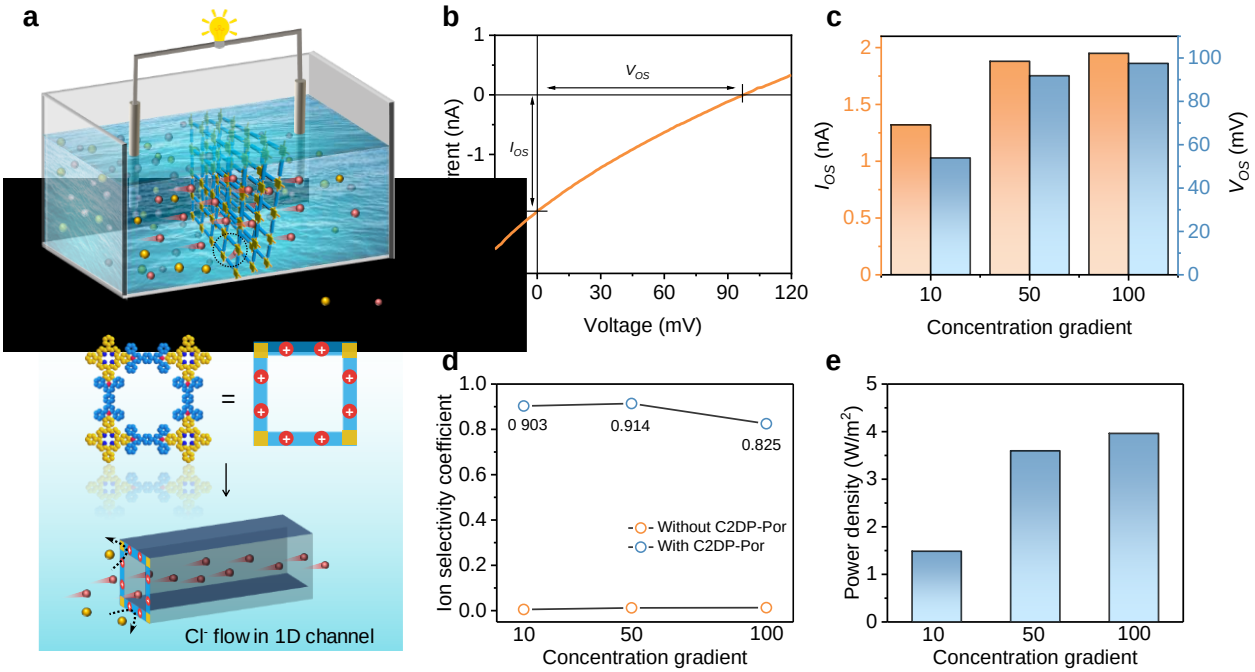

Fig. 4 | C2DP-Por-based osmotic power generation under salinity gradient. a, Schematic of the osmotic energy conversion process under a concentration gradient. **b**, *I-V* curve of the **C2DP-Por** film was recorded under 1/0.01 M KCl concentration gradient. **c**, Measured osmotic current and osmotic potential as a function of the transmembrane concentration gradient. The low concentration side is set to 0.01 M KCl. **d**, The **C2DP-Por** film shows good anion selectivity with a coefficient of about 0.83-0.9. **e**, Output power density as a function of the concentration gradient.

C2DP-Por single crystal for osmotic energy conversion. The achieved **C2DP-Por** possesses a high density of well-defined cationic skeleton (~ 2.4×10^6 C m^{-3}) and high density of inherent pores

Final edited form was published in "Nature Synthesis". 1 S. 69-76. ISSN: 2731-0582.
https://doi.org/10.1038/s44160-021-00001-4

(~ 1.1×10^{17} m^{-2}) combined with highly ordered quasi-1D channels, which can potentially contribute to excellent permselectivity and high diffusion flux of ions. In addition, the irreversible linkage provides high chemical stability and a robust framework structure (Supplementary Fig. 26-28), making **C2DP-Por** a promising candidate for the osmotic energy conversion from an ionic concentration gradient[21,27-29]. To evaluate the osmotic energy conversion behavior, the as-prepared **C2DP-Por** membrane with a thickness of 50 nm and crystal size of 40-100 μm^2 was transferred onto a silicon (Si) wafer which contains an open-hole of about 12 μm^2 in the centre for electrochemical current-voltage (*I*-*V*) measurement (Supplementary Fig. 29). Potassium chloride (KCl) was selected as the standard electrolyte because of the same diffusion coefficient of K^+ and Cl^- ions[30]. Under a transmembrane salinity gradient, the positively charged 2DP network with a high surface zeta potential of 135.4 mV (Supplementary Fig. 30) enables to selectively transport Cl^- ions, creating a net potential difference across the membrane (Fig. 4a). In order to eliminate the influence of redox potential produced by the unequal voltage drops on the electrode, standard saturated Ag/AgCl salt bridge electrodes were used[31]. As shown in Fig. 4b, the obtained *I*-*V* curve exhibits obvious intercepts on the *x* and *y* axis, which can be ascribed to the generated osmotic potential (V_{os}) and osmotic current (I_{os}). This is totally different from the blank supporting Si hole in which there is no contribution from the osmotic transport (Supplementary Fig. 31). As the concentration gradient increases, the I_{os} increases accordingly from 1.32 to 1.95 nA, while the V_{os} increases from 54 to 97 mV (Fig. 4c). The V_{os} can be described as:

$$V_{os} = S\frac{RT}{F}\Delta \mathrm{In}C$$

where *R*, *T*, and *F* are the universal gas constant, the absolute temperature, and the Faraday constant, respectively; $\Delta \mathrm{In}C$ is the natural logarithm of the salinity ratio between concentrated and diluted sides; *S* is the anion selectivity coefficient ranging from 0 to 1 (0 refers to non-selective case and

14

Final edited form was published in "Nature Synthesis". 1 S. 69-76. ISSN: 2731-0582.
https://doi.org/10.1038/s44160-021-00001-4

1 refers to ideally ion-selective case). It is defined as the difference of the transference number of anion and cation. The maximum selectivity coefficient can reach approximately 0.91 (corresponding to a Cl^-/K^+ selectivity ratio ~ 22) (Fig. 4d), which largely outperforms the previously reported single-layer MoS_2 nanopore[30]. It is also noteworthy that the selectivity coefficient decreases as salinity gradient increases, which is related to the decrease of Debye length upon increasing the ionic strength in the high concentration side. The output power density, calculated by $P = I_{os} \times V_{os}/4$, can reach as high as 4 W m^{-2} that outperforms the state-of-art 2D materials such as graphene and boron nitride (Fig. 4e and Supplementary Table 3)[32,33]. These results demonstrate for the first time that the crystalline 2DPs with intrinsic charged backbones and well-ordered nanopore channels can be utilized for the osmotic energy conversion.

Conclusions and outlook

In conclusion, we report the on-water surface synthesis of few-layer, large-area, single crystalline cationic 2DPs (**C2DPs**, including **C2DP-Por**, **C2DP-ZnPor**, and **C2DP-Py**) through an irreversible reaction assisted by surfactant monolayer. Model reactions—supported by theoretical calculation—demonstrate that manipulating pH in ring opening and ring closure steps enables the control of the reaction kinetics toward the targeted **C2DP** crystals. Further, we show that the **C2DP-Por** crystals with cationic skeleton and well-defined quasi-1D channels offer an excellent anion selectivity, thus ensuring high-performance osmotic energy generation under a salinity gradient. Our studies unlock a new avenue for synthesizing 2DP and 2D COF single crystals using kinetically-controlled irreversible reaction, and will propel the development of single-crystalline 2DPs. The selective nanofluidic transport capability could potentially endow **C2DP** with multiple unique functions ranging from membrane-based chemical-potential-gradient-driven energy

15

Final edited form was published in "Nature Synthesis". 1 S. 69-76. ISSN: 2731-0582.
https://doi.org/10.1038/s44160-021-00001-4

conversion technologies (e.g., photo-electric and thermo-electric conversion) to electrode protective layers for energy storage devices.

Methods

General characterization. ^{1}H, ^{13}C and ^{19}F NMR spectra were recorded at 30 °C on a Bruker Avance III 500 NMR spectrometer operating at 500.13 MHz for ^{1}H, 125.77 MHz for ^{13}C and 470.59 MHz for ^{19}F. Some NMR spectra were recorded at room temperature with a Bruker AV-II 300 spectrometer operating at 300.1 MHz for ^{1}H, 75.5 MHz for ^{13}C and 96.29 MHz for ^{11}B. DMSO-d_6 was used as solvent. The spectra were referenced on the solvent signal ($\delta(^{1}H)$ = 2.50 ppm; $\delta(^{13}C)$ = 39.6 ppm) or on external solution of C_6F_6 in DMSO-d_6 ($\delta(^{19}F)$ = -163 ppm). The ^{11}B NMR spectrum was referenced on the $BF_3{\cdot}Et_2O$ signal ($\delta(^{11}B)$ = 0 ppm) of an external standard. High resolution MALDI-TOF analyses were performed on Bruker Reflex II-TOF spectrometer using a 337-nm nitrogen laser with 2-[(2E)-3-(4-tert-Butylphenyl)-2-methylprop-2-enylidene]malononitrile (DCTB) as the matrix. Optical microscopy (Zeiss), Atomic force microscopy (AFM, NT-MDT), transmission electron microscopy (TEM, Zeiss, Libra 200 KV) and scanning electron microscopy (SEM, Zeiss Gemini 500) equipped with EDX was used to investigate the morphology and structure of the samples. Charged two-dimensional polymer (C2DP) films were deposited on Si substrate for SEM, and on copper grids for TEM characterizations. All optical microscopy and AFM images were recorded on a 300-nm SiO_2/Si substrate.

UV-visible absorption spectra of the polymers were obtained on a UV-Vis-NIR Spectrophotometer Cary 5000 at room temperature. FTIR spectra were collected using Tensor II (Bruker) with an attenuated total reflection (ATR) unit. The samples were prepared by depositing the 2D polymer films onto a copper foil. X-ray photoelectron spectroscopy (XPS) measurements

16

Final edited form was published in "Nature Synthesis". 1 S. 69-76. ISSN: 2731-0582.
https://doi.org/10.1038/s44160-021-00001-4

were carried out using an AXIS Ultra DLD system. Both surveys and high-resolution spectra were collected using a beam diameter of 100 μm. All displayed binding energy values are calibrated to the graphitic C1s peak with a value of 284.6 eV. Thin-film Grazing-incidence wide-angle X-Ray scattering (GIWAXS) data were acquired at European Synchrotron Radiation Facility (ESRF). The photon energy was 10 keV. The focused beam of ca. 0.3×0.3 mm^2 was directed on the sample at an incident angle α of 0.15° and 0.30°. Two-dimensional (2D) diffraction patterns were acquired by an X-ray area detector (MarCCD).

HRTEM imaging and image simulation. AC-HRTEM imaging was conducted on an FEI Titan 80-300 operated at 300 kV. The instrument is equipped with a hexapole aberration-corrector which corrects the geometrical axial aberrations up to the third-order. Due to the high sensitivity of organic 2D polymer crystals towards electron irradiation, we acquired HRTEM images under the low-dose mode so as to reduce the irradiation damage.

The unprocessed HRTEM image of C2DP and its fast Fourier transform (FFT) pattern are shown in Supplementary Fig. 20. The sharp reflections in the FFT pattern originate from the highly-ordered C2DP crystal. However, Thon rings were also observed, signalling beam-induced amorphization during image acquisition. Note that the electron dose for image acquisition was merely 70 $e^-/Å^2$, which significantly limits the signal-to-noise ratio in the HRTEM image obtained on a conventional CCD camera. In order to enhance the image contrast, we applied a defocus of several hundred nanometers. The exact defocus value was determined as follows.

First, we obtained the radial-integrated intensity profile of the FFT pattern. For amorphous material, the intensity of the FFT is proportional to the squared modulus of the phase contrast transfer function,

$$I_{\mathrm{FFT}} \propto \sin^2[2\pi\chi(q)]$$

17

Final edited form was published in "Nature Synthesis". 1 S. 69-76. ISSN: 2731-0582.
https://doi.org/10.1038/s44160-021-00001-4

where $\chi(q)$ is the wave aberration function, and q is the spatial frequency. If the anisotropic lens aberrations have been minimized via aberration correction, the wave aberration function in one dimension can be expressed by

$$\chi(q) = \frac{1}{2}C_1\lambda q^2 + \frac{1}{4}C_3\lambda^3 q^4 + \frac{1}{6}C_5\lambda^5 q^6$$

where C_1, C_3, and C_5 represent defocus, third-order spherical aberration and fifth-order spherical aberration, respectively.

Since we adjusted C_3 to -15 μm, and C_5 is fixed at 4 mm, the only variable in $\chi(q)$ is C_1. Therefore, C_1 can be determined by comparing the measured FFT intensity with the calculated $\sin^2[2\pi\chi(q)]$. The best-fitting defocus has been determined to be 420 nm. After determining the exact defocus, we performed image simulation using the QSTEM software. The simulated thickness-defocus map is shown in Supplementary Fig. 21.

DFT calculations of reaction energies. The Katritzky transamination reaction towards **C2DP-Por** and its lattice structures were studied with density functional theory (DFT) as implemented in the CP2K code [34]. The PBE exchange correlation functional[35] with DFT-D3 van der Waals corrections and Becke-Johnson damping were used[36]. The CP2K calculations used a mixed Gaussian and plane-wave basis set in combination with Goedecker-Teter-Hutter (GTH) pseudopotentials[37]. The double-ζ polarization MOLOPT basis set was used to describe H, C, N, B and F atoms. A plane-wave energy cutoff of 600 Ry was used for all the calculations. Three types of monolayer alignments were considered in the periodic crystal: AA stacking, inclined AA stacking and AB stacking for the cell parameter optimizations. For the reaction-formation calculations, acidic and basic conditions were considered by using explicit hydronium and hydroxide ion (H_3O^+ and OH^-) in the stationary geometry optimizations.

18

Final edited form was published in "Nature Synthesis". 1 S. 69-76. ISSN: 2731-0582.
https://doi.org/10.1038/s44160-021-00001-4

X-ray Diffraction Refinements. Suitable single crystals were coated with Paratone-N oil, mounted using a nylon loop and frozen in the cold nitrogen stream. A crystal was measured at 100 K on a Rigaku Oxford Diffraction SuperNova diffractometer using a Cu micro focus X-ray source. Crystal and data collection details are given in Supplementary Table 1. Data reduction and absorption correction were performed with CrysaAlisPro software[38]. Using Olex2 (ref.[39]), the structures were solved with SHELXT[40] by direct methods and refined with SHELXL[41] by least-square minimization against F^2 using first isotropic and later anisotropic thermal parameters for all non-hydrogen atoms. Hydrogen atoms bonded to carbon atoms were added to the structure models on calculated positions using the riding model. All other hydrogen atoms were localized in the difference Fourier map. Two tetrafluoroborate anions and one acetonitrile solvent molecule are disordered over two positions and were refined without further restraints. Images of the structures were produced with Olex2 (ref.[39]) software.

The X-ray crystallographic coordinates for the structure reported in this article have been deposited at the Cambridge Crystallographic Data Centre (CCDC), under CCDC deposition number 2000610. These data can be obtained free of charge from the CCDC via http://www.ccdc.cam.ac.uk/data_request/cif.

Synthesis of C2DP-Por through the surfactant monolayer assisted interfacial synthesis (SMAIS) method. 40 mL Milli-Q water was injected into a beaker (80 mL, diameter = 6 cm) to form a static air/water interface. Then, 10 μL SOS (1 mg mL^{-1} in chloroform) was spread onto the surface. The solvent was allowed to evaporate for 30 minutes, and then **9** (7.4×10^{-4} mmol in 1.75 M CH_3COOH aqueous solution) was gently added to the subphase using the syringe. After 2 h, 1.48×10^{-3} mmol **11** in aqueous solution and 1.75 mmol TEA were added successively. Then, the reaction was kept for 2 h, followed by the injection of 8.75 mmol CH_3COOH to the subphase.

Final edited form was published in "Nature Synthesis". 1 S. 69-76. ISSN: 2731-0582.
https://doi.org/10.1038/s44160-021-00001-4

The reaction mixture was then kept undistracted at 1 °C for 6 days. After the polymerization, the synthetic purple **C2DP-Por** film was deposited onto the substrate by the horizontal dipping method. The substrate with the **C2DP-Por** film was immersed in Milli-Q water for 5 min and rinsed with flowing ethanol, Milli-Q water, and then dried in N_2 flow.

Synthesis of C2DP-ZnPor through the SMAIS method. 40 mL Milli-Q water was injected into a beaker (80 mL, diameter = 6 cm) to form a static air/water interface. Then, 10 μL SOS (1 mg mL^{-1} in chloroform) was spread onto the surface. The solvent was allowed to evaporate for 30 minutes, and then **10** (6.8×10^{-4} mmol in 1.75 M CH_3COOH aqueous solution) was gently added to the subphase using the syringe. After 2 h, 1.36×10^{-3} mmol **11** in aqueous solution and 1.75 mmol TEA were added successively. Then, the reaction was kept for 2 h, followed by the injection of 8.75 mmol CH_3COOH to the subphase. The reaction mixture was then kept undistracted at 1 °C for 6 days. After the polymerization, the synthetic purple **C2DP-ZnPor** film was deposited onto the substrate by the horizontal dipping method. The substrate with the **C2DP-ZnPor** film was immersed in Milli-Q water for 5 min and rinsed with flowing ethanol, Milli-Q water, and then dried in N_2 flow.

Synthesis of C2DP-Py through the SMAIS method. 40 mL Milli-Q water was injected into a beaker (80 mL, diameter = 6 cm) to form a static air/water interface. Then, 10 μL SOS (1 mg mL^{-1} in chloroform) was spread onto the surface. The solvent was allowed to evaporate for 30 minutes, and then **12** (8.8×10^{-4} mmol in 1.75 M CH_3COOH aqueous solution) was gently added to the subphase using syringe. After 2 h, 1.77×10^{-3} mmol **11** in aqueous solution and 1.75 mmol TEA were added successively. Then, the reaction was kept for 2 h, followed by the injection of 8.75 mmol CH_3COOH to the subphase. The reaction mixture was then kept undistracted at 1 °C for 6 days. After the polymerization, the synthetic yellow **C2DP-Py** film was deposited onto the

20

Final edited form was published in "Nature Synthesis". 1 S. 69-76. ISSN: 2731-0582.
https://doi.org/10.1038/s44160-021-00001-4

substrate by the horizontal dipping method. The substrate with the **C2DP-Py** film was immersed in Milli-Q water for 5 min and rinsed with flowing ethanol, Milli-Q water, and then dried in N_2 flow.

Electrochemical measurement. C2DP-Por film with a thickness of approximately 50 nm was transferred onto a Si wafer which contains an open-hole in the centre. As shown in Supplementary Fig. 27, the hole has a small opening of ~12 μm^2 and a large opening of several hundred micrometres. The Si wafer with polymer membrane was further mounted between a custom-made two-compartment electrochemical cell. The electrochemical current-voltage (*I-V*) measurement was performed with an electrochemical workstation (*CHI*). Potassium chloride (KCl) was selected as the standard electrolyte because of the same diffusion coefficient of K^+ and Cl^- ions. All the testing solutions were prepared using ultrapure water (18.2 MΩ cm). In order to eliminate the influence of redox potential produced by the unequal voltage drops on the electrode, saturated Ag/AgCl salt bridge electrodes were used (*HANA Instrument*)[31]. Different from the blank Si substrate, after the transfer of **C2DP-Por** membrane, obvious intercepts were observed in the *I-V* curves, indicating that the 2DP membrane can act as an osmotic power generator due to its intrinsic charged backbones.

Data availability

The data supporting the findings of this study are available within the Article and its Supplementary Information or from the corresponding author upon reasonable request.

References

1 Feng, X. & Schlüter, A. D. Towards macroscopic crystalline 2D polymers. *Angew. Chem., Int. Ed.* **57**, 13748-13763 (2018).

2 Côté, A. P. et al. Porous, crystalline, covalent organic frameworks. *Science* **310**, 1166-1170

(2005).

3 Wang, H. et al. Recent progress in covalent organic framework thin films: fabrications, applications and perspectives. *Chem. Soc. Rev.* **48**, 488-516 (2019).

4 Colson, J. W. et al. Oriented 2D covalent organic framework thin films on single-layer graphene. *Science* **332**, 228-231 (2011).

5 Martínez-Abadía, M. et al. A wavy two-dimensional covalent organic framework from core-twisted polycyclic aromatic hydrocarbons. *J. Am. Chem. Soc.* **141**, 14403-14410 (2019).

6 Xu, H., Gao, J. & Jiang, D. Stable, crystalline, porous, covalent organic frameworks as a platform for chiral organocatalysts. *Nat. Chem.* **7**, 905-912 (2015).

7 Seo, J.-M., Noh, H.-J., Jeong, H. Y. & Baek, J.-B. Converting unstable imine-linked network into stable aromatic benzoxazole-linked one via post-oxidative cyclization. *J. Am. Chem. Soc.* **141**, 11786-11790 (2019).

8 Liu, K. et al. On-water surface synthesis of crystalline, few-layer two-dimensional polymers assisted by surfactant monolayers. *Nat. Chem.* **11**, 994-1000 (2019).

9 Wojtecki, R. J., Meador, M. A. & Rowan, S. J. Using the dynamic bond to access macroscopically responsive structurally dynamic polymers. *Nat. Mater.* **10**, 14-27 (2011).

10 Ma, T. et al. Single-crystal X-ray diffraction structures of covalent organic frameworks. *Science* **361**, 48-52 (2018).

11 Kory, M. J. et al. Gram-scale synthesis of two-dimensional polymer crystals and their structure analysis by X-ray diffraction. *Nat. Chem.* **6**, 779-784 (2014).

12 Jin, E. et al. Two-dimensional sp^2 carbon–conjugated covalent organic frameworks. *Science* **357**, 673-676 (2017).

13 Zhuang, X. et al. A two-dimensional conjugated polymer framework with fully sp^2-bonded carbon skeleton. *Polym. Chem.* **7**, 4176-4181 (2016).

14 Lyu, H., Diercks, C. S., Zhu, C. & Yaghi, O. M. Porous crystalline olefin-linked covalent organic frameworks. *J. Am. Chem. Soc.* **141**, 6848-6852 (2019).

15 Jadhav, T. et al. 2D Poly(arylene vinylene) covalent organic frameworks via aldol condensation of trimethyltriazine. *Angew. Chem., Int. Ed.* **58**, 13753-13757 (2019).

16 Pastoetter, D. L. et al. Synthesis of vinylene-linked two-dimensional conjugated polymers via the horner–wadsworth–emmons reaction. *Angew. Chem., Int. Ed.* **59**, 23620 (2020).

17 Liu, W. et al. A two-dimensional conjugated aromatic polymer via C–C coupling reaction. *Nat. Chem.* **9**, 563-570 (2017).

18 Galeotti, G. et al. Synthesis of mesoscale ordered two-dimensional π-conjugated polymers with semiconducting properties. *Nat. Mater.* **19**, 874–880 (2020).

19 Grill, L. et al. Nano-architectures by covalent assembly of molecular building blocks. *Nat. Nanotechnol.* **2**, 687-691 (2007).

20 Clair, S. & de Oteyza, D. G. Controlling a chemical coupling reaction on a surface: tools and strategies for on-surface synthesis. *Chem. Rev.* **119**, 4717-4776 (2019).

21 Zhu, X. et al. A charge-density-tunable three/two-dimensional polymer/graphene oxide heterogeneous nanoporous membrane for ion transport. *ACS Nano* **11**, 10816-10824 (2017).

22 Chen, C. et al. Bio-inspired nanocomposite membranes for osmotic energy harvesting. *Joule* **4**, 247-261 (2020).

23 Harris, F. W., Chuang, K. C., Huang, S. A. X., Janimak, J. J. & Cheng, S. Z. D. Aromatic poly(pyridinium salt)s: synthesis and structure of organo-soluble, rigid-rod poly(pyridinium tetrafluoroborate)s. *Polymer* **35**, 4940-4948 (1994).

Final edited form was published in "Nature Synthesis". 1 S. 69-76. ISSN: 2731-0582.
https://doi.org/10.1038/s44160-021-00001-4

24 Katritzky, A. R., Manzo, R. H., Lloyd, J. M. & Patel, R. C. Mechanism of the pyrylium/pyridinium ring interconversion. mild preparative conditions for conversion of amines into pyridinium ions. *Angew. Chem., Int. Ed.* **19**, 306-306 (1980).

25 Katritzky, A. R. & Leahy, D. E. Kinetics and mechanism of the pyrylium to pyridinium cation transformation in dichloromethane. *J. Chem. Soc., Perkin Trans. 2*, 171-174 (1985).

26 Yan, X., Augusti, R., Li, X. & Cooks, R. G. Chemical reactivity assessment using reactive paper spray ionization mass spectrometry: the Katritzky reaction. *ChemPlusChem* **78**, 1142-1148 (2013).

27 Cheng, C., Jiang, G., Simon, G. P., Liu, J. Z. & Li, D. Low-voltage electrostatic modulation of ion diffusion through layered graphene-based nanoporous membranes. *Nat. Nanotechnol.* **13**, 685-690 (2018).

28 Logan, B. E. & Elimelech, M. Membrane-based processes for sustainable power generation using water. *Nature* **488**, 313-319 (2012).

29 Siria, A., Bocquet, M.-L. & Bocquet, L. New avenues for the large-scale harvesting of blue energy. *Nat. Rev. Chem.* **1**, 0091 (2017).

30 Feng, J. et al. Single-layer MoS_2 nanopores as nanopower generators. *Nature* **536**, 197-200 (2016).

31 Esfandiar, A. et al. Size effect in ion transport through angstrom-scale slits. *Science* **358**, 511-513 (2017).

32 Ji, J. et al. Osmotic power generation with positively and negatively charged 2D nanofluidic membrane pairs. *Adv. Funct. Mater.* **27**, 1603623 (2017).

33 Zhang, Z. et al. Oxidation promoted osmotic energy conversion in black phosphorus membranes. *Proc. Natl. Acad. Sci.* **117**, 13959-13966 (2020).

34 Kühne, T. D. et al. CP2K: an electronic structure and molecular dynamics software package - quickstep: efficient and accurate electronic structure calculations. *J. Chem. Phys.* **152**, 194103 (2020).

35 Petersen, A. C., Crockett, L., Richards, M. & Boxer, A. A self-report measure of pubertal status: reliability, validity, and initial norms. *J. Youth Adolesc.* **17**, 117-133 (1988).

36 Smith, D. G. A., Burns, L. A., Patkowski, K. & Sherrill, C. D. Revised damping parameters for the D3 dispersion correction to density functional theory. *J. Phys. Chem. Lett.* **7**, 2197-2203 (2016).

37 Goedecker, S., Teter, M. & Hutter, J. Separable dual-space gaussian pseudopotentials. *Phys. Rev. B* **54**, 1703-1710 (1996).

38 CrysAlisPRO, Oxford Diffraction/Agilent Technologies UK Ltd, Yarnton, England.

39 Dolomanov, O. V., Bourhis, L. J., Gildea, R. J., Howard, J. A. K. & Puschmann, H. OLEX2: a complete structure solution, refinement and analysis program. *J. Appl. Cryst.* **42**, 339-341 (2009).

40 Sheldrick, G. A short history of SHELX. *Acta Cryst.* **64**, 112-122 (2008).

41 Sheldrick, G. Crystal structure refinement with SHELXL. *Acta Cryst. C* **71**, 3-8 (2015).

Acknowledgments

This work is financially supported by EU Graphene Flagship (GrapheneCore3, No. 881603), ERC starting grant (FC2DMOF, No. 852909), ERC Consolidator Grant (T2DCP), DFG project (2D polyanilines, No. 426572620), Coordination Networks: Building Blocks for Functional Systems (SPP 1928, COORNET), H2020-MSCA-ITN (ULTIMATE, No. 813036), H2020-FETOPEN (PROGENY, 899205), CRC 1415 (Chemistry of Synthetic Two-Dimensional Materials, No.

417590517), SPP 2244 (2DMP), as well as the German Science Council and Center of Advancing Electronics Dresden (cfaed). Z. W. gratefully acknowledges funding from China Scholarship Council. The authors acknowledge cfaed and Dresden Center for Nanoanalysis (DCN) at TUD and Dr. Petr Formanek, Prof. Andreas Fery for the use of TEM facility at IPF.

Author contributions

X.F. and R.D. conceived and designed the project. Z.W., M.W., L.W., K.X. and R.D. contributed to the synthesis of 2D polymers and model compounds. Z.Z. and Z.W. contributed to the osmotic power generation measurements. H.Q., Z.W., R.D. and U.K. performed AC-HRTEM imaging, SAED and the corresponding analysis. Z.W. and S.P. contributed to the GIWAXS measurement. Z.W., H.Q. and R.D. analyzed the diffraction data and proposed the crystal structures. Z.W. performed optical microscopy, AFM, TEM, ATR-FTIR and UV-vis measurements. A.O., A.D., A.C. and G.C. contributed to the theory calculations and analysis. F.H. and J.W. performed the single crystalline X-ray measurement and analysis. H.K. performed the NMR measurements on model compound. Z.W., R.D. and X.F. co-wrote the manuscript, with contributions from all authors.

Competing interests

The authors declare no competing interests.

Additional information

Supplementary information is available for this paper at https://

Correspondence and requests for materials should be addressed to R.D. or X.F.

Reprints and permissions information is available at http://